Journal of the European Ceramic Society 40 (2020) 3431–3436

Contents lists available at ScienceDirect

Journal of the European Ceramic Society

journal homepage: www.elsevier.com/locate/jeurceramsoc

Original Article

Anisotropy of the grain size effect on the electrical resistivity of *n*-type $Bi_{1.9}Gd_{0.1}Te_3$ thermoelectric textured by spark plasma sintering

Oleg Ivanov[a,b,*], Maxim Yaprintsev[a], Alexei Vasil'ev[a]

[a] Belgorod State University, Belgorod, 308015, Russia
[b] Belgorod State Technological University named after V.G. Shukhov, Belgorod, 308012, Russia

ARTICLE INFO

Keywords:
Bismuth telluride
Spark plasma sintering
Textured grain structure
Electrical resistivity
Grain size effect

ABSTRACT

Spark plasma sintering (SPS) was applied to prepare textured $Bi_{1.9}Gd_{0.1}Te_3$ compounds with various grain structures, tuned by changing in the sintering temperature. The grains forming ordered lamellar structure under texturing are elongated in plane oriented perpendicularly to SPS-pressing direction. As result, average grain size measured parallel to this direction and corresponding to fine-grained samples happened to be much less as compared to relevant size for perpendicular direction characteristic for coarse-grained samples. Anisotropy in electrical resistivity inherent for single crystal was found to be partially recovered in textured samples, i.e. resistivity measured along directions parallel or perpendicular to SPS-pressuring direction is different. Moreover, resistivity for both directions is increasing with decreasing in grain size or with decreasing in intergrain distance. Grain size effect on resistivity due to grain boundary scattering of electrons was found to be anisotropic, since the effect is observed for different ranges of change in average grain sizes.

1. Introduction

It is known that grain boundaries in grained metals and semiconductors can act as effective scattering centers for electrons [1–4]. Generally, the grain boundary scattering results in increasing in the specific electrical resistivity, ρ, via relevant decreasing in mobility of electrons. In this case, ρ will naturally be dependent on intergrain spacing. Usually, grain size effect on ρ is well expressed for nano- and micrograined conducting solids. To find and analyze this effect, the electrical properties of the grained samples with various grain sizes corresponding to nano- and micro scale should be examined. Desired grain structure can be usually tuned during a preparation of the grained samples by varying some technological variables. The grained samples used to research the grain size effect on ρ are usually characterizing by random orientation of the grains. Due to chaotic grain arrangement, the physical properties of these samples are isotropic. Besides, average grain size, measured in any direction, will be the same. That is the grain size effect on ρ in the isotropic grained samples with completely random orientation of the grains is isotropic effect. To get a preferential grain orientation, the grained samples should be textured. Under texturing, the grains are dominantly ordered in some crystal plane positioned perpendicularly to texturing axis. If compound being textured possess itself an inherent anisotropy in the physical properties characteristic for single crystal, the texturing can recover, at least, partially, this anisotropy in the textured samples. It means that the properties, measured along directions parallel or perpendicular to the texturing axis, will be rather different. Moreover, the grain sizes for these directions can be happened to be different, too. In this case, a number of the grain boundaries overcome by the electrons taking part in the electrical conductivity should be different for the parallel or perpendicular directions that will result in anisotropy of the grain size effect on the electrical resistivity. Besides this difference in number of the grain boundaries, ability of these boundaries to scatter the electrons can be also different for both directions mentioned additionally effecting on the grain size effect on ρ. It is known that the grained Bi_2Te_3 compound can be readily texturing during preparation processes based on uniaxial loading applied to an initial powder under compacting and sintering [5–14]. Therefore, this compound can be reasonably chosen to examine anisotropy of the grain size effect on the electrical resistivity in the textured materials. It is important to note that at present the Bi_2Te_3-based alloys of *n*- and *p*-conductivities are main low-temperature thermoelectric materials, directly conversing thermal energy into electricity. Efficiency of the conversion is characterized by the thermoelectric figure-of-merit, $ZT = TS^2/\rho k$, where T is the absolute temperature, S is the Seebeck coefficient and k is the total thermal conductivity. The texturing is remarkably effecting on ρ and k, and, hence, ZT, of the grained Bi_2Te_3-based compounds. Thus, the texturing can be considered as additional parameter governing the thermoelectric

* Corresponding author at: Belgorod State University, Belgorod, 308015, Russia.
E-mail address: Ivanov.Oleg@bsu.edu.ru (O. Ivanov).

https://doi.org/10.1016/j.jeurceramsoc.2020.03.048
Received 3 February 2020; Received in revised form 18 March 2020; Accepted 22 March 2020
Available online 29 March 2020
0955-2219/

properties (ρ and k) of these compounds to enhance their thermoelectric efficiency. A few technological ways can be applied to texture the Bi_2Te_3 and Bi_2Te_3-based alloys including extrusion, hot pressing, spark plasma sintering. Particularly, spark plasma sintering was successfully applied to prepare the n-type textured $Bi_{1.9}Gd_{0.1}Te_3$ compounds with various grain structures differing in shape and size of the grains [11]. Therefore, these compounds are suitable to find and analyze anisotropy of the grain size effect on the electrical resistivity in grained thermoelectrics. It is known that rare earth elements, R, (R = Lu, Ce, Sm, Er, La, Gd, etc.) can be successfully used as donor dopants to remarkably enhance the thermoelectric performance of Bi_2Te_3 [15–25]. Therefore, in the compounds being studied Gd was also using as dopant just to enhance ZT. However, here we will not discuss the Gd-doping effect on the thermoelectric properties of Bi_2Te_3. Only the grain size effect on the electrical resistivity of the textured $Bi_{1.9}Gd_{0.1}Te_3$ compounds will be under detailed examination.

2. Materials and methods

Microwave-solvothermal synthesis was used to prepare a starting $Bi_{1.9}Gd_{0.1}Te_3$ powder. Synthesis conditions were reported in detail in Ref. [11,26]. Spark plasma sintering method by using a SPS-25/10 system was applied to compact the starting powder at pressure of 40 MPa and sintering time of 150 s resulting in the Ø20 mm × 15 mm cylinders. Different SPS-temperatures, T_S, equal to 690, 720, 735, 750, 780, and 810 K were used to prepare the samples with various grain structures [11].

To observe starting powder morphology and estimate particles size, a model JEM - 2100 transmission electron microscope (TEM) was used. X-ray diffraction (XRD) analysis was performed by using a Rigaku Ultima IV diffractometer with CuK_α – radiation to estimate a texturing degree of the samples with various T_S via calculating an orientation factor. To examine changing in Te content due to its high-temperature evaporation during the SPS-process, a Shimadzu ICP (Inductively Coupled Plasma) emission spectrometer ICPE-9000 was applied. A Nova NanoSEM 450 scanning electron microscope (SEM) was applied to study grain structures features and estimate average grain size. The specific electrical resistivity of the 2 × 2 × 10 mm bar samples was measured by using a ZEM-3 system. A Mini Cryogen Free Measurements System (Cryogenic Ltd, UK) was used to study the Hall effect and estimate the concentration, n, and Hall mobility, μ_H, of electrons.

3. Results and discussion

Before analyzing the grain size effect on the electrical resistivity of the textured $Bi_{1.9}Gd_{0.1}Te_3$ compounds, it would be helpful to briefly consider main features of these compounds reported earlier in Ref. [11]. XRD pattern for the starting $Bi_{1.9}Gd_{0.1}Te_3$ powder is shown in Fig. 1 (a). This XRD pattern is corresponding to single hexagonal phase characteristic for pure Bi_2Te_3 (PDF#01 − 089-4302).

All the diffraction peaks can be exactly indexed with the standard diffraction planes in accordance with the space symmetry $R\bar{3}m$ group. It is important to note that the starting powder mainly consisted of hexagonal plates with average plate size of a few hundreds of nm and width of ~100 nm. A few of typical hexagonal plates are shown in the TEM-image in inset to Fig. 1(a). Therefore, the plates should be considered as 2D-particles. Forming the 2D-plates during a chemical synthesis of Bi_2Te_3 compound is known to be directly related to specific features in crystal structure and chemical bonding of this compound [27,28]. The crystal structure is layered one, and crystal $a – b$ planes are oriented along the layers, whereas crystal c-axes are perpendicular to the layers. The chemical bonding between atoms within the layers is dominantly strong covalent, whereas neighboring layers are bonded via weak Van-der-Waals interaction. Due to various nature of the chemical bonding along and between the layers, a growth of the Bi_2Te_3 particles during synthesis happens to be 2D, since growth rates are different for

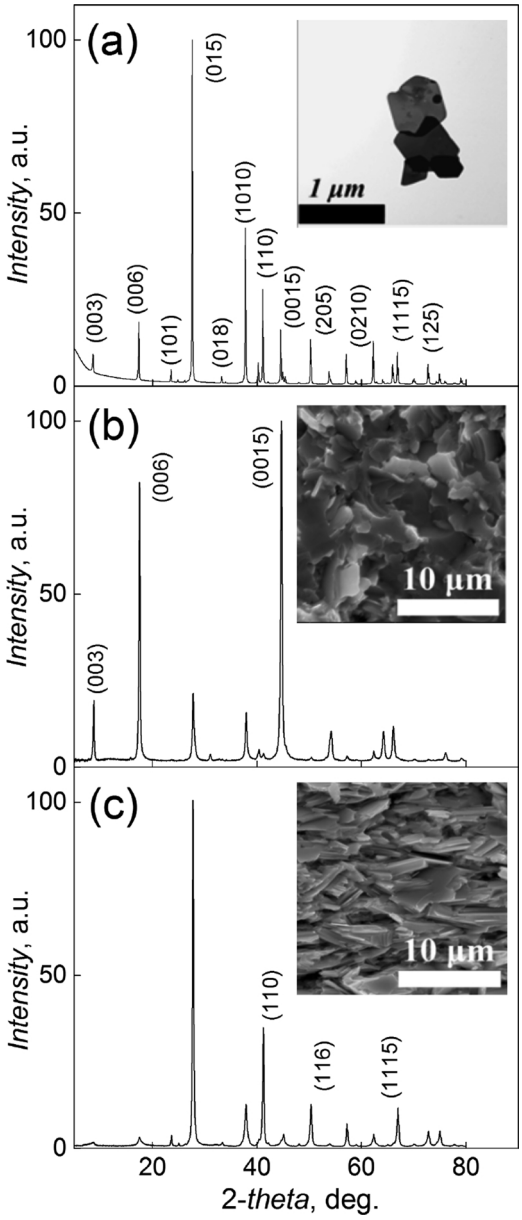

Fig. 1. (a) XRD pattern for the starting $Bi_{1.9}Gd_{0.1}Te_3$ powder (inset shows the TEM-image of the particles in the starting powder; (b) XRD pattern for the bulk sample sintered at T_S = 810 K and taken on surface oriented perpendicularly to the SPS-pressing direction; (c) XRD pattern for the same bulk sample taken on surface oriented parallel to the SPS-pressing direction. Insets to Fig. (b) and (c) show SEM-images taken on the fractured surfaces oriented perpendicularly and parallel to the SPS-pressing direction for the textured samples sintered at 810 K, respectively.

directions parallel and perpendicular to the layers. XRD pattern presented in Fig. 1(a) is corresponding to the powder with completely random 2D-plates orientation. If a bulk material prepared from this starting powder will be consisted of grains chaotically arranged, XRD pattern for the bulk material will be coincided with XRD pattern for the relevant bulk material. Hence, XRD patterns for the disordered powder and the disordered bilk material will be same. However, under texturing the grains start to being ordered in some plane oriented perpendicularly to the texturing axis. As a result, preferential orienting of crystal planes reflecting X-ray radiation will take place. In turn, XRD patterns collected on fractured surfaces oriented parallel or perpendicularly to the texturing axis can be remarkably different. This difference is related to redistribution in the intensities of some peaks of two XRD

patterns. Such kind of redistribution was really observed in bulk grained $Bi_{1.9}Gd_{0.1}Te_3$ samples spark-plasma-sintered at various temperatures, and the texturing degree happened to be T_S-dependent. The texturing axis was found to be oriented along crystal 001 direction and parallel to the SPS-pressing direction. XRD patterns collected on fractured surfaces oriented parallel or perpendicularly to the applied SPS-pressing direction for the sample with $T_S = 810$ K are shown in Fig. 1(b) and (c), respectively. Although positions of all the peaks in these XRD patterns are corresponding to rhombohedral $R\bar{3}m$ structure, the intensities of (00*l*) and (11*l*) peaks are strongly dependent on the SPS-pressing direction. For XRD pattern taken for surface oriented perpendicularly to the SPS-pressing direction, the intensities of the (00*l*) peaks are remarkably enhancing (Fig. 1(b)), whereas the intensities of the (11*l*) peaks are in turn increasing in XRD pattern taken for other pressing direction (Fig. 1(c)). The redistribution in the intensities is originated from forming a lamellar texture characterizing by preferential orientation of the grains. In the textured samples, *c*-axes of the grains are preferentially directed parallel to the SPS-pressing direction, while *a*-*b* planes of the grains are preferentially oriented perpendicularly to this direction. XRD patterns similar to ones presented in Fig. 1(b) and (c) for the sample with $T_S = 810$ K were also analyzed for the samples SPS-prepared at all other T_S. All the samples were found to be highly textured along the 001 direction parallel to the SPS-pressing direction. Degree of preferential grain orientation for the textured samples can be estimated by an orientation factor, *F*, given by [9]

$$F = \frac{p - p_0}{1 - p_0} \tag{1}$$

where p and p_0 are defined as

$$p = \frac{I(00l)}{\sum I(hkl)}, \text{ and } p_0 = \frac{I_0(00l)}{\sum I_0(hkl)} \tag{2}$$

Here, the I_0 and I intensities are corresponding to non-oriented (non-textured) and oriented (textured) samples, respectively. Naturally, $F = 0$ is for completely non-oriented samples (powder or grained material with completely random grain orientation). Under gradual developing the texturing, *F* starts to be increased and becomes equal to 1 for completely oriented samples (like single crystal). Next, XRD patterns were applied to calculate the p and p_0 values and, hence, estimate *F* for all the samples.

The texturing observed in XRD patterns was also confirmed by analyzing SEM-images of the grain structures recorded on the fractured surfaces oriented perpendicularly (inset to Fig. 1(b)) or parallel (inset to Fig. 1(c)) to the SPS-pressing direction. At the fractured surfaces perpendicular the SPS-pressing direction, disordered grain structure with a few μm grains having mainly irregular shape is observed. However, at the fractured surfaces parallel to this direction, the grains form ordered lamellar structure, and the lamellar sheets lie in plane perpendicular to the SPS-pressing direction. Therefore, one can conclude that SEM-images of the grain structures presented in the insets are well consistent with XRD patterns presented in Fig. 1(a) and (b). It is important to note that the lamellar sheets consist of the grains elongated in the plane oriented perpendicularly to the SPS-pressing direction. The schematic of the texturing for the sample studied is shown in Fig. 2. Each grain is assumed to be an ellipsoid to plot this schematic.

Therefore, the grain can be imaged as an ellipse in the plane parallel to the SPS-pressing direction. The orientation of *c*-axis and *a*–*b* plane in an individual grain is also shown. It is important to note that *c*-axes of the grains are preferentially directed parallel to the SPS-pressing direction, whereas *a*–*b* planes of the grains are preferentially oriented perpendicularly to the SPS-pressing direction. As a result, the grain sizes in the directions parallel and perpendicular to the SPS-pressing direction are rather different.

To estimate average grain size in both directions, the histograms of the grain size distribution were plotted for the samples with various T_S. Average grain sizes, corresponding to directions parallel ($D_\parallel$) and

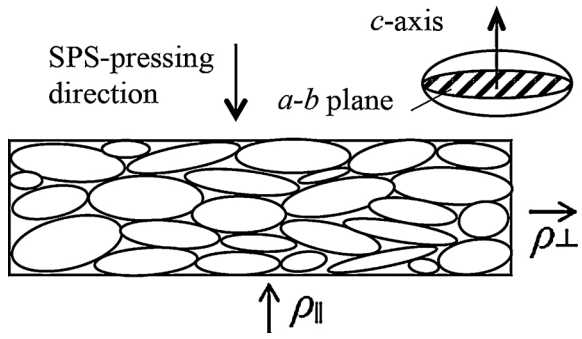

Fig. 2. The schematic of the texturing developing during the SPS-process.

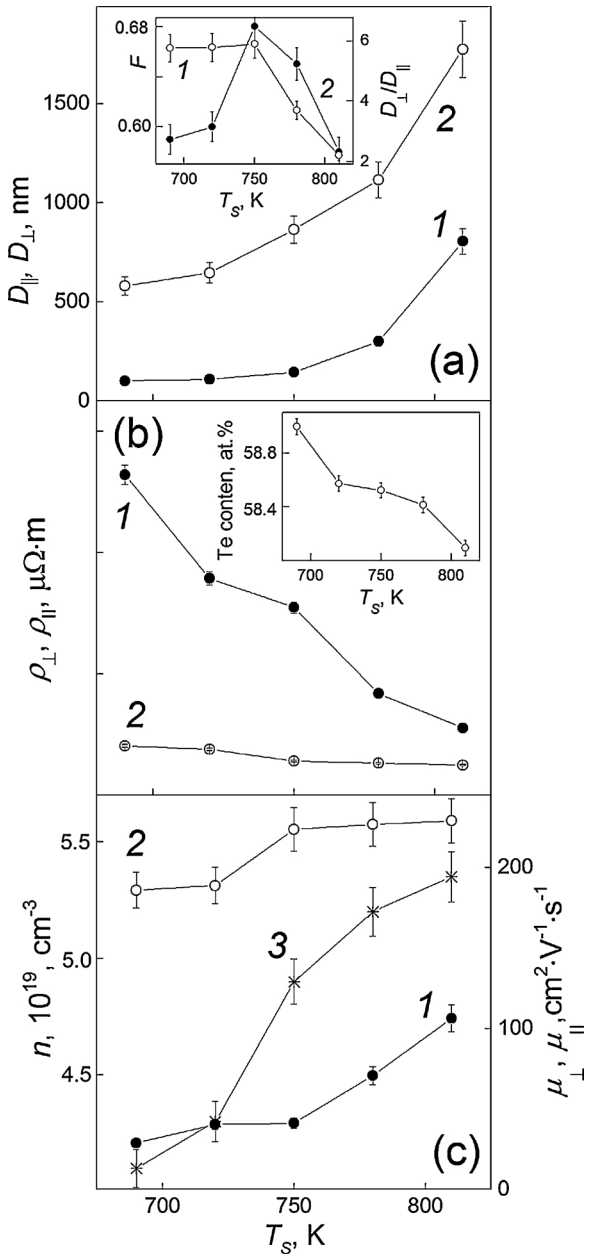

Fig. 3. (a) The $D_\parallel$ (curve *1*) and $D_\perp$ (*2*) vs. T_S dependences. Inset: the $D_\perp/D_\parallel$ (*1*) and *F* (*2*) vs. T_S dependences; (b) The $\rho_\perp$ (*1*) and $\rho_\parallel$ (*2*) vs. T_S dependences. Inset: the Te content vs. T_S dependence; (c) The $\mu_{H\parallel}$ (*1*), $\mu_{H\perp}$ (*2*) and *n* (*3*) vs. T_S dependences.

perpendicular ($D_\perp$) to the SPS-pressing direction, were next estimated by analyzing the histograms in frames of the lognormal unimodal distribution [29]. The $D_\parallel(T_S)$ and $D_\perp(T_S)$ dependences are presented in Fig. 3(a). One can see that the $D_\perp$ values happened to be much bigger as compared to the $D_\parallel$ values. In addition, both average sizes were found to be steady increasing with increasing T_S. Taking into account big enough difference in $D_\parallel$ and $D_\perp$, the samples examined along the SPS-pressing direction can be considered as coarse-grained samples, whereas the samples examined perpendicularly to the SPS-pressing direction are rather corresponding to fine-grained samples. So, the texturing allows combining the properties of the coarse-grained and fine-grained materials in the same sample. A grain shape factor, $D_\perp/D_\parallel$, can be introduced to characterize the difference in the grain sizes measured for both directions in the textured samples. The $D_\perp/D_\parallel(T_S)$ dependence along with the $F(T_S)$ dependence are presented in inset to Fig. 3(a). With increasing T_S, both dependences are firstly increased for $T_S \leq 750$ K, but then they start to fall for $T_S \geq 750$ K. Therefore, these quantities are maximal at $T_S = 750$ K. It can be reasonably assumed that ability of a grained material to being textured under the SPS-process will be dependent on the grain shape factor of the growing grains. The starting 2D (plates) or 1D (whiskers) particles usually form the shape-anisotropic grains with big grain shape factor in the relevant bulk materials. During the SPS-process, such shape-anisotropic grains are preferentially arranged in the plane oriented perpendicularly to the applied SPS-pressing direction resulting to the texturing. The texturing releases a strain created by the high uniaxial pressuring. However, any arranging in 3D-isotropic grained system will be far less probable, since this arranging in the isotropic system will not release this strain. Thus, forming the shape-anisotropic grains with big grain shape factor is favoring to sinter the textured material with big orientation factor.

As was mentioned above, crystal Bi_2Te_3 structure is layered one. The physical properties, measured parallel or perpendicularly to the layers are rather different. For instance, anisotropy coefficient in the electrical resistivity, ρ_c/ρ_{ab}, of the Bi_2Te_3 and Bi_2Te_3-based single crystals is equal to $\sim 5 \div 5.5$ [12,13,30]. Here *ab* and *c* subscripts corresponds to the ρ measuring directions oriented either along crystal *a* – *b* plane or along crystal *c*-axis, respectively. For grained material with completely random orientation of the grains, the electrical resistivity will be independent on the measuring directions. The texturing developing at the SPS-process results in recovering in anisotropy in the specific electrical resistivity of the grained $Bi_{1.9}Gd_{0.1}Te_3$ samples. Moreover, ρ happens to be T_S-dependent. The T_S-effect on ρ measured at 290 K for the parallel orientation measuring, $\rho_\parallel$, (measuring ρ is in direction parallel to the SPS-pressing direction) and for the perpendicular orientation measuring, $\rho_\perp$, (ρ is measured perpendicularly to the SPS-pressing direction) is shown in Fig. 3(b). The electrical resistivity for the parallel orientation measuring (curve *1*) is much more as compared to the perpendicular orientation measuring (*2*). Both $\rho_\parallel$ and $\rho_\perp$ are steady decreasing with increasing T_S. It is known that the specific electrical resistance of a donor semiconductor can be expressed as $\rho = 1/(e\mu n)$, where *e* is the electron charge [31]. Usually, the grain size effect on the resistivity can be attributed to changing in electron mobility due to additional grain boundary scattering in grained materials. However, in the samples studied various grain structures with different grain sizes were formed via the SPS-process. Since the SPS-process is implemented at high temperatures, changing in the electrical resistivity of these samples can be also originated from, firstly, changing in electron concentration and, secondly, forming other defects, but the grain boundaries. Therefore, the $\rho(T_S)$ changes in Fig. 3(b) can be originated from the relevant $\mu(T_S)$ and $n(T_S)$ changes. Due to anisotropy in ρ for the textured samples, two values of the Hall mobility corresponding to the perpendicular ($\mu_{H\perp}$) and parallel ($\mu_{H\parallel}$) orientations should be measured. The $n(T_S)$, $\mu_{H\perp}(T_S)$ and $\mu_{H\parallel}(T_S)$ dependences are presented in Fig. 3(c). Both the electron concentration and the Hall mobilities are increasing with increasing T_S demonstrating a rather complicated behavior. The $\mu_{H\perp}$ mobility is much bigger than $\mu_{H\parallel}$, whereas *n* is the same for both

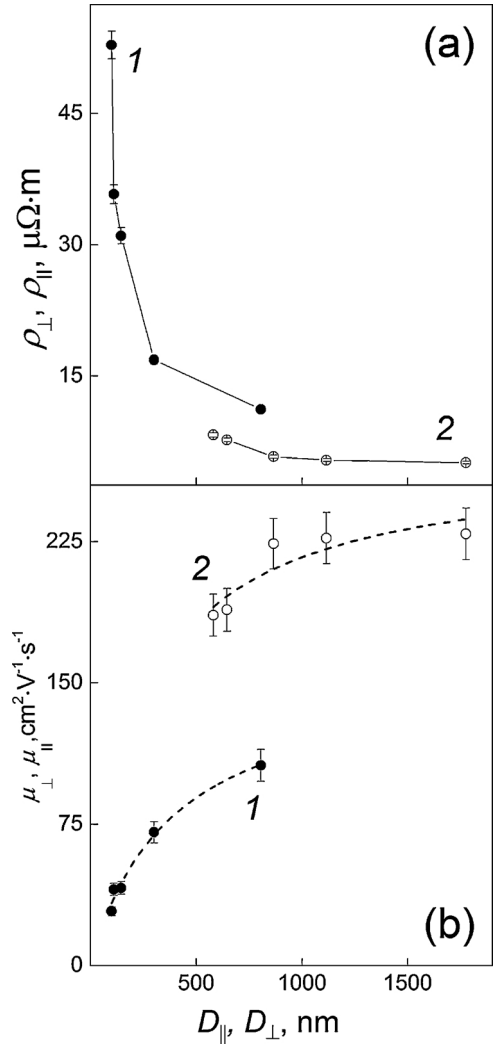

Fig. 4. (a) The $\rho_\parallel(D_\parallel)$ – curve *1*, and $\rho_\perp(D_\perp)$ – *2* dependences; (b) The $\mu_{H\parallel}(D_\parallel)$ – *1*, and $\mu_{H\perp}(D_\perp)$ - *2* dependences. The dashed lines are the fitting curves corresponding to the Mayadas–Shatzkes model.

parallel and perpendicular orientations. Increasing in *n* with increasing T_S can be related to high-temperature Te evaporation resulting in forming the vacancies at Te sites, $V_{Te}^{\bullet\bullet}$ [32–34]. In turn, forming each positively charged $V_{Te}^{\bullet\bullet}$ vacancy is accompanied by appearing two free electrons in accordance with equation

$$Bi_2Te_3 = 2Bi_{Bi}^{\times} + 2Te_{Te}^{\times} + Te(g) + V_{Te}^{\bullet\bullet} + 2e' \quad (3)$$

where symbol g is corresponding to a gaseous phase.

For the samples studied, the Te content was really found to be gradually decreasing with increasing T_S, as is shown in inset to Fig. 3(b). Since energy of Te evaporation (52.55 kJ·mol^{-1}) is much lower than that of Bi (104.80 kJ·mol^{-1}) [18], at high temperatures Te is evaporated much easier than Bi. The Te evaporation will be enhancing with increasing T_S. In turn, in accordance with Eq. (3) electron concentration should be increasing with decreasing Te content (or with increasing in number of the Te vacancies), that was confirmed experimentally.

Data of the Fig. 3(a) and (b) were used to plot the $\rho_\parallel(D_\parallel)$ and $\rho_\perp(D_\perp)$ dependences (Fig. 4 (a)). Both the electrical resistivities are growing with decreasing in the grain sizes, i.e. the grain size effect on the electrical resistivity takes place. Since this effect is corresponding to different ranges of the $D_\parallel$ and $D_\perp$ changes, it can be attributed to anisotropy of the grain size effect. The $\mu_{H\parallel}(D_\parallel)$ and $\mu_{H\perp}(D_\perp)$ dependences are shown in Fig. 4(b). The electrical resistivity and electron mobility

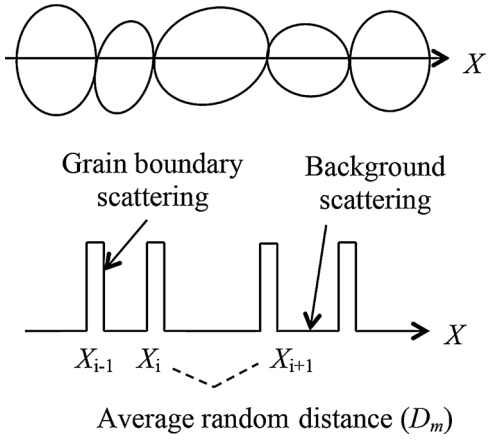

Fig. 5. 1D-chain of the grains (top) and potential $V(X)$ barriers (bottom) corresponding to the grain boundaries.

are changed in opposite manner. The grain size effect on $\rho_{\parallel}$ and $\rho_{\perp}$ (or on $\mu_{H\parallel}$ and $\mu_{H\perp}$) is much more pronounced for the parallel orientation measuring, which is corresponding to the fine-grained samples. Moreover, one can conclude that this effect is remarkably enhancing at transition from the micrograined to nanograined samples. The $\mu_{H\perp}$ mobility is clearly saturated at $D_{\perp} \geq \sim 1000$ nm, i.e. the grain boundary scattering becomes ineffective for the coarse-grained samples.

Is should be noted that besides the grain size effect, changing in electron mobility can be also originated from forming the $V_{Te}^{\bullet\bullet}$ vacancies during the SPS-process, which are other scattering centers for the electrons. However, in this case the mobilities should be decreasing with increasing T_S, since the Te content is steady decreasing with increasing T_S (inset to Fig. 3(b)), that is in contradiction with experimental data (Fig. 3(b)). Changing in $\rho_{\parallel}$ and $\rho_{\perp}$ with varying T_S could be also related to recovering in natural anisotropy of the mobilities under the texturing. In this case, the $\mu_{H\perp}(T_S)$ and $\mu_{H\parallel}(T_S)$ dependences should be correlated with the $F(T_S)$ dependence (curve *2* in inset to Fig. 2(a)), i.e. both Hall mobilities should have maxima at $T_S = 750$ K, that is again in contradiction with experimental data. Thus, the grain size effect on the electron mobility seems to be dominant mechanism governing the changing in ρ in the textured $Bi_{1.9}Gd_{0.1}Te_3$ samples SPS-prepared at different T_S.

To analyze the grain boundaries effect on ρ, presented in Fig. 4, the Mayadas-Shatzkes model can be involved [35,36]. According to this 1D-model, the grain boundaries are represented by N parallel planes, oriented perpendicular to the direction of the constant electric field, E, with average separation $d = D_m$. At the X_n position of the n-th plane, there is a potential barrier, which has to be overcome by the free electrons taking part in the electrical conductivity and drifting under electrical field along X-direction (Fig. 5).

Generally, the grain boundary effect on the electrical resistivity depends on average grain size, D_m, electron men free path, l_e, and reflectivity, R, of the grain boundaries. The l_e path is due to electron scattering by phonons and defects, except for the grain boundaries, i.e. l_e is the background mean free path. The R reflectivity characterizes the fraction of electrons that is scattered from the potential barriers. The D_m, l_e and R parameters can be combined in α coefficient in accordance with expression

$$\alpha = \frac{mS^2}{\hbar^3 D_m k_F} 2\tau = \frac{l_e}{D_m} \bullet \frac{R}{1-R} \tag{4}$$

where m is the electron mass, $\hbar$ is the reduced Planck constant, and k_F is the magnitude of the Fermi wavevector.

The scattering electron processes from the potential barriers will results in increasing in ρ via relevant decreasing in μ. The D_m-effect on μ can be presented by expression

$$\mu_g = 3\left[\frac{1}{3} - \frac{1}{2}\bullet\alpha + \alpha^2 - \alpha^3 \bullet ln\left(1 + \frac{1}{\alpha}\right)\right]\bullet\mu_0 \tag{5}$$

where μ_0 is D_m-independent mobility, characteristic for a grainless material, and μ_g is D_m-dependent mobility taking into account the grain boundary contribution to the total resistivity of a grained material.

The experimental $\mu_{H\parallel}(D_{\parallel})$ and $\mu_{H\perp}(D_{\perp})$ curves can satisfactorily be reproduced by expression (6), as shown by the dashed lines in Fig. 4(b). The fitting parameters in expression (6) were taken as μ_0 and $A = l_e R/(1\text{-}R)$. These parameters were estimated to be equal to $\mu_{0\parallel} = 160\ \mathrm{cm^2 \cdot V^{-1} \cdot s^{-1}}$ and $A_{\parallel} = 285$ nm, and $\mu_{0\perp} = 270\ \mathrm{cm^2 \cdot V^{-1} \cdot s^{-1}}$ and $A_{\perp} = 170$ nm for the parallel (the fine-grained samples) and perpendicular (the coarse-grained samples) orientations measuring. It would be very interesting to extract the $R_{\parallel}$ and $R_{\perp}$ values for both orientations measuring. To do so, the $l_{e\parallel}$ and $l_{e\perp}$ values corresponding to the parallel and perpendicular orientations measuring should be used. Unfortunately, at present these values are unknown. Since the orientation factor for the textured samples studied is much less unit, using literature data for $l_{e\parallel}$ and $l_{e\perp}$ would be incorrect. However, let us take into account that in any case the electron mobility is obviously proportional to the electron mean free path. Then, one can believe that the $\mu_{0\parallel} \sim l_{e\parallel}$ and $\mu_{0\perp} \sim l_{e\perp}$ links are correct. Therefore, using the A definition one can come to the equality of the following ratios

$$\frac{A_{\parallel}\bullet\mu_{\perp}}{A_{\perp}\bullet\mu_{\parallel}} = \left(\frac{R_{\parallel}}{1-R_{\parallel}}\right)/\left(\frac{R_{\perp}}{1-R_{\perp}}\right) \tag{6}$$

Using the fitting parameters, left part of this equation was calculated as ~ 0.88, which is close enough to 1. Hence, the $R_{\parallel}$ and $R_{\perp}$ values are seemed to be very close to each other.

4. Conclusion

Thus, the textured $Bi_{1.9}Gd_{0.1}Te_3$ samples were prepared by the SPS-process. The grain size was tuned by varying in the sintering temperature. Due to texturing, the grain sizes measured parallel to the SPS-pressing direction (the fine-grained samples) happened to be much bigger as compared to that measured perpendicular to this direction (the coarse-grained samples). Anisotropy in the electrical resistivity, measured along these directions, was found and analyzed in the frames of the Mayadas-Shatzkes model. This anisotropy is originated from big difference in the intergrain distance for the parallel or perpendicular orientation measuring which, in turn, is resulting in different contribution of the grain boundary scattering to the total resistivity. The grain size effect on the resistivity is remarkably enhancing at transition from micrograined to nanograined samples.

Declaration of Competing Interest

The authors declare that they have no known competing financial interests or personal relationships that could have appeared to influence the work reported in this paper.

Acknowledgements

M. Y. thanks Russian Foundation for Basic Research for the financial support under project No 18-32-00415. All of studies were carried out by the scientific equipment of joint research center "Technologies and Materials" at the Belgorod State University.

References

[1] Q.G. Zhang, X. Zhang, B.Y. Cao, M. Fujii, K. Takahashi, T. Ikuta, Influence of grain boundary scattering on the electrical properties of platinum nanofilms, Appl. Phys. Lett. 89 (2006) 114102-114102-3.
[2] H. Zeng, Y. Wu, J. Zhang, C. Kuang, M. Yue, S. Zhou, Grain size-dependent

electrical resistivity of bulk nanocrystalline Gd metals, Prog. Nat. Sci. Mater. Int. 23 (2013) 18–22.
[3] O. Ivanov, O. Maradudina, R. Lyubushkin, Grain size effect on electrical resistivity of bulk nanograined Bi_2Te_3 material, Mater. Charact. 99 (2015) 175–179.
[4] S. Riedel, J. Röber, T. Geßner, Electrical properties of copper films produced by MOCVD, Microelectr. Eng. 33 (1997) 165–172.
[5] S.D. Bhame, D. Pravarthana, W. Prellier, J.G. Noudem, Enhanced thermoelectric performance in spark plasma textured bulk n-type $Bi_2Te_{2.7}Se_{0.3}$ and p-type $Bi_{0.5}Sb_{1.5}Te_3$, Appl. Phys. Lett. 102 (2013) 2190-1-3.
[6] X.A. Fan, J.Y. Yang, R.G. Chen, H.S. Yun, W. Zhu, S.Q. Bao, X.K. Duan, Characterization and thermoelectric properties of p-type 25%Bi_2Te_3–75%Sb_2Te_3 prepared via mechanical alloying and plasma activated sintering, J. Phys. D Appl. Phys. 39 (2006) 740–745.
[7] J. Jiang, L. Chen, S. Bai, Q. Yao, Q. Wang, Fabrication and thermoelectric performance of textured n-type $Bi_2(Te,Se)_3$ by spark plasma sintering, Mater. Sci. Eng. B 117 (2005) 334–338.
[8] Q. Lognon, F. Gascoin, O.I. Lebedev, L. Lutterotti, S. Gascoin, D. Chateigner, Quantitative texture analysis of spark plasma textured *n*-Bi_2Te_3, J. Am. Ceram. Soc. 97 (2014) 2038–2045.
[9] A. Vasil'ev, M. Yaprintsev, O. Ivanov, E. Danshina, Anisotropic thermoelectric properties of $Bi_{1.9}Lu_{0.1}Te_{2.7}Se_{0.3}$ textured via spark plasma sintering, Sol. St. Sci. 84 (2018) 28–43.
[10] Y. Morisaki, H. Araki, H. Kitagawa, M. Orihashi, K. Hasezaki, K. Kimura, Bi_2Te_3-related thermoelectric samples with aligned-texture prepared by plastic deformation, Mater. Trans. 46 (2005) 2518–2524.
[11] M. Yaprintsev, A. Vasil'ev, O. Ivanov, Thermoelectric properties of the textured $Bi_{1.9}Gd_{0.1}Te_3$ compounds spark-plasma-sintered at various temperatures, J. Eur. Ceram. Soc. 40 (2020) 742–750.
[12] O. Ben-Yehuda, R. Shuker, Y. Gelbstein, Z. Dashevsky, M.P. Dariel, Highly textured Bi_2Te_3-based materials for thermoelectric energy conversion, J. Appl. Phys. 101 (2007) 113707-1 - 6.
[13] J.J. Shen, L.P. Hu, T.J. Zhu, X.B. Zhao, The texture related anisotropy of thermoelectric properties in bismuth telluride based polycrystalline alloys, Appl. Phys. Lett. 99 (2011) 124102-1 - 3.
[14] X. Yan, B. Poudel, W.S. Liu, G. Joshi, H. Wang, Y. Lan, D. Wang, G. Chen, Z.F. Ren, Experimental studied on anisotropic thermoelectric properties and structures of n-type $Bi_2Te_{2.7}Se_{0.3}$, Nano Lett. 10 (2010) 3373–3378.
[15] J. Yang, F. Wu, Z. Zhu, L. Yao, H. Song, X. Hu, Thermoelectrical properties of lutetium-doped Bi_2Te_3 bulk samples prepared from flower-like nanopowders, J. Alloys Compd. 619 (2015) 401–405.
[16] X.H. Ji, X.B. Zhao, Y.H. Zhang, B.H. Lu, H.L. Ni, Synthesis and properties of rare earth containing Bi_2Te_3 based thermoelectric alloys, J. Alloys Compd. 387 (2005) 282–286.
[17] F. Wu, H. Song, J. Jia, X. Hu, Effects of Ce, Y, and Sm doping on the thermoelectric properties of Bi_2Te_3 alloy, Prog. Nat. Sci. Mater. Int. 23 (2013) 408–412.
[18] F. Wu, W. Shi, X. Hu, Preparation and thermoelectric properties of flower-like nanoparticles of Ce-Doped Bi_2Te_3, Electron. Mater. Lett. 11 (2015) 127–132.
[19] X.H. Ji, X.B. Zhao, Y.H. Zhang, B.H. Lu, H.L. Ni, Solvothermal synthesis and thermoelectric properties of lanthanum contained Bi–Te and Bi–Se–Te alloys, Mater. Lett. 59 (2005) 682–685.
[20] F. Wu, H.Z. Song, J.F. Jia, F. Gao, Y.J. Zhang, X. Hu, Thermoelectric properties of Ce-doped n-type $Ce_xBi_{2-x}Te_{2.7}Se_{0.3}$ nanocomposites, Phys. Stat. Sol. A 210 (2013) 1183–1189.
[21] W.Y. Shi, F. Wu, K.L. Wang, J.J. Yang, H.Z. Song, X.J. Hu, Preparation and thermoelectric properties of yttrium-doped Bi_2Te_3 flower-like nanopowders, Electron. Mater. 43 (2014) 3162–3168.
[22] X.B. Zhao, Y.H. Zhang, X.H. Ji, Solvothermal synthesis of nano-sized $La_xBi_{(2-x)}Te_3$ thermoelectric powders, Inorg. Chem. Commun. 7 (2004) 386–388.
[23] O. Ivanov, M. Yaprintsev, R. Lyubushkin, O. Soklakova, Enhancement of thermoelectric efficiency in Bi_2Te_3 via rare earth element doping, Scr. Mater. 146 (2018) 91–94.
[24] M. Yaprintsev, R. Lyubushkin, O. Soklakova, O. Ivanov, Effects of Lu and Tm doping on thermoelectric properties of Bi_2Te_3, J. Electron. Mater. 47 (2018) 1362–1370.
[25] O. Ivanov, M. Yaprintsev, Mechanisms of thermoelectric efficiency enhancement in Lu-doped Bi_2Te_3, Mater. Res. Express 5 (2018) 015905-1-10.
[26] M. Yapryntsev, A. Vasil'ev, O. Ivanov, Sintering temperature effect on thermoelectric properties and microstructure of the grained $Bi_{1.9}Gd_{0.1}Te_3$ compound, J. Eur. Ceram. Soc. 39 (2019) 1193–1205.
[27] H.J. Goldsmid, Bismuth telluride and its alloys as materials for thermoelectric generation, Materials. 7 (2014) 2577–2592.
[28] H. Scherrer, S. Scherrer, Thermoelectrics Handbook: Macro to Nano, CRC Taylor and Francis, Boca Raton, 2012.
[29] F.J. Humphreys, M. Hatherly, Recrystallization and Related Annealing Phenomena, Elsevier, Oxford, 2004.
[30] G.S. Nolas, J. Sharp, H.J. Goldsmid, Thermoelectrics Basic Principles and New Materials Developments, Springer, Berlin, 2001.
[31] J. Seo, K. Park, D. Lee, C. Lee, Microstructure and thermoelectric properties of *p*-type $Bi_{0.5}Sb_{0.5}Te_{0.5}$ compounds fabricated by hot pressing and hot extrusion, Scr. Mater. 38 (1998) 477–484.
[32] Y. Pan, T.R. Wei, C.F. Wu, J.F. Li, Electrical and thermal transport properties of spark plasma sintered n-type $Bi_2Te_{3-x}Se_x$ alloys: the combined effect of point defect and Se content, J. Mater. Chem. C. 3 (2015) 10583–10589.
[33] L. Hu, T. Zhu, X. Liu, X. Zhao, Point defect engineering of high-performance bismuth-telluride-based thermoelectric materials, Adv. Funct. Mater. 24 (2014) 5211–5218.
[34] J. Suh, K.M. Yu, D. Fu, X. Liu, F. Yang, J. Fan, D.J. Smith, Y.H. Zhang, J.K. Furdyna, C. Dames, W. Walukiewicz, J. Wu, Simultaneous enhancement of electrical conductivity and thermopower of Bi_2Te_3 by multifunctionality of native defects, Adv. Mater. 27 (2015) 3681–3686.
[35] A.V. Mayadas, M. Shatzkes, Electrical-resistivity model for polycrystalline films: the case of arbitrary reflection at external surfaces, Phys. Rev. B 1 (1970) 1382–1388.
[36] D. Choi, M. Moneck, X. Liu, S.J. Oh, C.R. Kagan, K.R. Coffey, K. Barmak, Crystallographic anisotropy of the resistivity size effect in single crystal tungsten nanowires, Sci. Rep. 3 (2013) 2591-1-4.